11-1-2016

Coupling of Coronal and Heliospheric Magnetohydrodynamic Models: Solution Comparisons and Verification

V. G. Merkin
Johns Hopkins University

R. Lionello
Predictive Science, Inc., San Diego

J. G. Lyon
Dartmouth College

J. Linker
Predictive Science, Inc., San Diego

T. Török
Predictive Science, Inc., San Diego

See next page for additional authors

The Astrophysical Journal, 831:23 (14pp), 2016 November 1 doi:10.3847/0004-637X/831/1/23

COUPLING OF CORONAL AND HELIOSPHERIC MAGNETOHYDRODYNAMIC MODELS: SOLUTION COMPARISONS AND VERIFICATION

V. G. Merkin[1], R. Lionello[2], J. G. Lyon[3], J. Linker[2], T. Török[2], and C. Downs[2]
[1] The Johns Hopkins University Applied Physics Laboratory, Laurel, MD 20723, USA; slava.merkin@jhuapl.edu
[2] Predictive Science, Inc., San Diego, CA 92121, USA
[3] Department of Physics and Astronomy, Dartmouth College, Hanover, NH 03755, USA
Received 2016 March 18; revised 2016 July 23; accepted 2016 August 8; published 2016 October 24

ABSTRACT

Two well-established magnetohydrodynamic (MHD) codes are coupled to model the solar corona and the inner heliosphere. The corona is simulated using the MHD algorithm outside a sphere (MAS) model. The Lyon–Fedder–Mobarry (LFM) model is used in the heliosphere. The interface between the models is placed in a spherical shell above the critical point and allows both models to work in either a rotating or an inertial frame. Numerical tests are presented examining the coupled model solutions from 20 to 50 solar radii. The heliospheric simulations are run with both LFM and the MAS extension into the heliosphere, and use the same polytropic coronal MAS solutions as the inner boundary condition. The coronal simulations are performed for idealized magnetic configurations, with an out-of-equilibrium flux rope inserted into an axisymmetric background, with and without including the solar rotation. The temporal evolution at the inner boundary of the LFM and MAS solutions is shown to be nearly identical, as are the steady-state background solutions, prior to the insertion of the flux rope. However, after the coronal mass ejection has propagated through the significant portion of the simulation domain, the heliospheric solutions diverge. Additional simulations with different resolution are then performed and show that the MAS heliospheric solutions approach those of LFM when run with progressively higher resolution. Following these detailed tests, a more realistic simulation driven by the thermodynamic coronal MAS is presented, which includes solar rotation and an azimuthally asymmetric background and extends to the Earth's orbit.

Key words: magnetohydrodynamics (MHD) – solar wind – Sun: corona – Sun: coronal mass ejections (CMEs) – Sun: heliosphere

1. INTRODUCTION

Coronal mass ejections (CMEs) are the largest disturbances in the heliosphere in terms of their mass, momentum, and kinetic energy. They can contain more than a billion tons of mass (e.g., Vourlidas et al. 2002), and a fast CME can have a speed in excess of 2000 km s^{-1} (Gopalswamy 2006; Gopalswamy et al. 2009). CMEs are eruptions of material from the solar atmosphere that can cause strong perturbations of the planetary magnetospheres on their way, as they propagate through the interplanetary space. Due to their immense scale and energy budget, CMEs have been the focus of solar–terrestrial physics for at least four decades (e.g., Gosling et al. 1974).

CMEs are known to be the primary drivers of the most intense geomagnetic storms on Earth (Tsurutani et al. 1988; Gosling et al. 1990; Richardson et al. 2001) and of solar energetic particle (SEP) events (Reames 1999, 2013). Understanding and eventually predicting space weather thus entails studying diverse plasma processes at various stages of CME formation and evolution, starting with their initiation in the corona and further propagation through interplanetary space (e.g., Forbes et al. 2006; Jacobs & Poedts 2011).

For the past two decades, the primary workhorses for such studies have been magnetohydrodynamic (MHD) models, which have seen significant progress since the early attempts dating back to the 1980s (e.g., Dryer et al. 1989). Initial approaches inserted a hydrodynamic disturbance at the inner boundary of the heliospheric model, which would then interact with the ambient solar wind and interplanetary magnetic field, as it propagated through the heliosphere (Detman et al. 1991; Wu et al. 1996; Odstrcil & Pizzo 1999). The same approach later became known as the "cone model" method (Xie et al. 2004) widely used today (e.g., Odstrcil et al. 2004a; Odstrcil & Pizzo 2009; Taktakishvili et al. 2009; Lee et al. 2013). Recently, similar ad hoc methods have been used including a spheromak magnetic field structure (Kataoka et al. 2009; Shiota & Kataoka 2016).

A different approach to simulating CMEs in the heliosphere is to simulate both the corona and the inner heliosphere from first principles. Such models can include the corona and the heliosphere either in one physical domain (Usmanov & Dryer 1995; Wu et al. 1999; Groth et al. 2000; Manchester et al. 2004b; Lugaz et al. 2005; Shen et al. 2007, 2013) or with two domains coupled at the interface (e.g., Odstrcil et al. 2002a; Riley et al. 2002; Tóth et al. 2005; Wu et al. 2007; Lionello et al. 2013).

MHD models have been used to address many aspects of CME propagation physics, i.e., the effects of CME-initiated shock waves on the background plasma and fields (e.g., Odstrcil et al. 2002a; Luhmann et al. 2004), CME kinematics and energy budget (e.g., Manchester et al. 2004a, 2004b), mass evolution (e.g., Lugaz et al. 2005), deformation as a result of interaction with the ambient solar wind (e.g., Odstrcil et al. 2004b; Wu et al. 2007), and interaction of multiple CMEs (e.g., Lugaz et al. 2005, 2007, 2008; Shen et al. 2011, 2012, 2013; Lugaz & Farrugia 2014). In addition to understanding basic MHD properties of CME initiation and propagation, such models are also instrumental in interpreting observations of the three-dimensional (3D) CME structure and SEP events by multi-spacecraft missions such as *STEREO* (Aschwanden et al. 2006; Lugaz et al. 2009; Rouillard et al. 2011).

In the present work, we report on a new effort aimed at time-dependent coupling of dedicated first-principles models of the

corona and the heliosphere for CME propagation. This approach affords the advantage of allowing different numerical techniques for treatment of the different physical regimes of the coronal and solar wind plasmas (e.g., implicit versus explicit numerical schemes, decoupling of the different time step constraints pertaining to the two physical domains) and the capability to maintain separate development tracks for the different numerical codes while retaining the coupling infrastructure (Odstrcil et al. 2004a).

The models used herein are the MHD algorithm outside a sphere (MAS) code (e.g., Linker et al. 1999; Mikić et al. 1999) of the corona and the heliospheric version of the Lyon–Fedder–Mobarry (LFM) MHD code (Lyon et al. 2004), LFM-helio (Merkin et al. 2011; Pahud et al. 2012; Merkin et al. 2016). The key advantage of the LFM numerics for simulations of the inner heliosphere plasmas is their high resolving power, allowing efficient capturing of sharp solution features such as MHD shocks and discontinuities. For the sake of simplicity, in this work, we consider mostly LFM simulations of CMEs driven by polytropic coronal MAS solutions. However, the MAS 3D MHD thermodynamic code, which includes coronal heating, anisotropic thermal conduction, and radiative losses, can provide more realistic simulations of the global plasma density and temperature structure of the corona and of the solar wind (Lionello et al. 2009). We demonstrate an LFM simulation of a CME driven by the thermodynamic coronal MAS at the end of the paper.

The coronal MAS and LFM codes are coupled at an interface located above the height where the solar wind becomes supersonic and super-Alfvénic (the critical point), near 20 solar radii ($R_\odot$). In order to test the coupled model performance, we build upon the work of Lionello et al. (2013; RL13 hereafter), who used a heliospheric version of the MAS code to propagate CME transients first simulated in the corona by the coronal MAS code. Here, we initiate the LFM heliospheric simulation at its inner boundary from the coronal MAS code and then compare the resulting heliospheric solutions during different stages of CME propagation against the heliospheric MAS simulations of RL13.

The rest of the paper is structured as follows. Section 2 describes the numerical models used. Section 3 outlines our methodology for coupling the coronal and heliospheric models. In Section 4, we present the results of our simulations, including tests with non-rotating and rotating axisymmetric background, as well as a more realistic CME simulation. Finally, Section 5 summarizes and concludes the paper.

2. MODEL DESCRIPTIONS

This section briefly describes the numerical models used herein, starting with LFM-helio, followed by the MAS code description.

2.1. LFM-helio

The details of the LFM code numerics were given by Lyon et al. (2004). In brief, the code solves the ideal MHD equations on an arbitrary hexahedral grid using a total variance diminishing scheme of the eighth order. A more recent version of the code also includes an explicit resistivity term (Merkin et al. 2015). The heliospheric version of the LFM code (LFM-helio) was originally used for steady-state solar wind calculations (Merkin et al. 2011; Pahud et al. 2012), but has recently been improved to include time-dependent coronal boundary conditions (Merkin et al. 2016). The work presented herein utilizes a similar time-dependent coronal boundary condition. In addition, in contrast to the previous works by Merkin et al. (2011) and Pahud et al. (2012), LFM-helio now solves the entire 3D domain extending all the way to the poles, which may be important for particularly large geoeffective CMEs. Among other advances is the possibility of performing the calculations in both inertial and rotating frames. The basic set of equations that the LFM code solves are as follows.

$$\frac{\partial \rho}{\partial t} + \nabla \cdot (\rho \boldsymbol{v}) = 0, \tag{1}$$

$$\frac{\partial (\rho \boldsymbol{v})}{\partial t} + \nabla \cdot (\rho \boldsymbol{v}\boldsymbol{v} + p\boldsymbol{I}) + \nabla \cdot \left(\frac{B^2}{8\pi}\boldsymbol{I} - \frac{\boldsymbol{B}\boldsymbol{B}}{4\pi}\right) + \rho\left(\frac{GM_\odot}{r^2}\hat{\boldsymbol{r}} + 2\boldsymbol{\Omega} \times \boldsymbol{v} - \boldsymbol{\Omega} \times \boldsymbol{r} \times \boldsymbol{\Omega}\right) = 0, \tag{2}$$

$$\frac{\partial}{\partial t}\left(\frac{\rho v^2}{2} + \frac{p}{\gamma - 1}\right) + \nabla \cdot \left[\boldsymbol{v}\left(\frac{\rho v^2}{2} + \frac{\gamma}{\gamma - 1}p\right)\right] + \boldsymbol{v} \cdot \nabla \cdot \left(\frac{B^2}{8\pi}\boldsymbol{I} - \frac{\boldsymbol{B}\boldsymbol{B}}{4\pi}\right) + \rho\boldsymbol{v} \cdot \left(\frac{GM_\odot}{r^2}\hat{\boldsymbol{r}} - \boldsymbol{\Omega} \times \boldsymbol{r} \times \boldsymbol{\Omega}\right) = 0, \tag{3}$$

$$\frac{\partial \boldsymbol{B}}{\partial t} = \nabla \times (\boldsymbol{v} \times \boldsymbol{B}) \tag{4}$$

where t and $\boldsymbol{r}$ are time and radial position vector; ρ, $\boldsymbol{v}$, p, and $\boldsymbol{B}$ are plasma density, velocity, pressure, and magnetic field, respectively, in the corotating frame; $\boldsymbol{I}$ is the unity matrix; $\boldsymbol{\Omega}$ is the solar angular velocity; $\hat{\boldsymbol{r}}$ is the unit vector in the radial direction; G is the gravitational constant; γ is the polytropic index, and $M_\odot$ is the solar mass. When the simulations are performed in the inertial frame, we set $\boldsymbol{\Omega} = 0$. As discussed by Lyon et al. (2004), the energy equation is written for the plasma —not total—energy, which is beneficial in small plasma β regions, such as the inner magnetosphere, but may not be as important in the solar wind.

2.2. MAS

For brevity, we denote the coronal MAS code "MAS-c" and the heliospheric MAS code "MAS-h" hereafter. As explained in more detail in RL13, both versions solve the 3D, time-dependent, MHD equations (Lionello et al. 1998, 1999; Mikić et al. 1999) in a computational domain extending between $r_{\min} \leqslant r \leqslant r_{\max}$:

$$\boldsymbol{\nabla} \times \boldsymbol{B} = \frac{4\pi}{c}\boldsymbol{J}, \tag{5}$$

$$\boldsymbol{\nabla} \times \boldsymbol{A} = \boldsymbol{B}, \tag{6}$$

$$\frac{\partial \boldsymbol{A}}{\partial t} = \boldsymbol{v} \times \boldsymbol{B} - \frac{c^2\eta}{4\pi}\boldsymbol{\nabla} \times \boldsymbol{B}, \tag{7}$$

$$\frac{1}{\gamma - 1}\left(\frac{\partial T}{\partial t} + \boldsymbol{v} \cdot \boldsymbol{\nabla} T\right) = -T\boldsymbol{\nabla} \cdot \boldsymbol{v} + \frac{m}{k\rho}S, \tag{8}$$

$$\rho\left(\frac{\partial \boldsymbol{v}}{\partial t} + \boldsymbol{v}\cdot\nabla\boldsymbol{v}\right) = \frac{1}{c}\boldsymbol{J}\times\boldsymbol{B} - \nabla p + \rho\boldsymbol{g} + \nabla\cdot(\nu\rho\nabla\boldsymbol{v}) + \boldsymbol{F}_{\rm fict}, \quad (9)$$

where $\boldsymbol{B}$ is the magnetic field, $\boldsymbol{J}$ is the electric current density, $\boldsymbol{A}$ is the vector potential, ρ, $\boldsymbol{v}$, p, and $T = T_i + T_e = 2T_i$ are the plasma mass density, velocity, pressure, and temperature, where T_i and T_e are ion and electron temperatures, $\boldsymbol{g} = -g_0 R_\odot^2 \hat{\boldsymbol{r}}/r^2$ is the gravitational acceleration ($g_0 = GM_\odot/R_\odot^2$), η the resistivity, and ν is the kinematic viscosity. The continuity equation is not reproduced here because it is identical to (1). In the inertial frame of reference, the fictitious force term, $\boldsymbol{F}_{\rm fict}$, is absent. In the rotating frame of reference, we have

$$\boldsymbol{F}_{\rm fict} = -\rho[2\boldsymbol{\Omega}\times\boldsymbol{v} + \boldsymbol{\Omega}\times(\boldsymbol{\Omega}\times\boldsymbol{r})]. \quad (10)$$

Here, the first term on the right-hand side is the Coriolis force, while the second term is the centrifugal force. Both depend on the angular velocity $\boldsymbol{\Omega}$. Thus, Equation (9) is mathematically equivalent to (2) with the addition of the viscous term. S in Equation (8) represents the energy sources term.

The MAS model is capable of using the full thermodynamic treatment of Lionello et al. (2009; which includes collisionless thermal conduction). However, for most simulations in this work (Sections 4.1, 4.2.1, 4.2.2, and 4.2.3), we use the so-called polytropic approximation as in Linker et al. (2003), which prescribes a simple adiabatic energy equation (i.e., $S = 0$, which is appropriate in the heliosphere), and choose a suitable value for γ. In Section 4.2.4, we present a heliospheric LFM simulation driven by the thermodynamic MAS-c model.

3. MAS–LFM COUPLING METHODOLOGY

Similarly to previous efforts (Odstrcil et al. 2002b), the coupling between the two codes is achieved by overlapping the ghost region of the lower boundary of the heliospheric code and the active physical domain of the coronal code. Figure 1 demonstrates this schematically. The red arc represents the lower boundary of the active physical domain of the heliospheric code, referred to as the boundary interface hereafter. The shaded region below the boundary interface is the ghost region of the heliospheric code, where the boundary conditions are set. Note that the blue grid representing the coronal code need not end at the boundary interface and may extend further out. What is important is that plasma flow be super-fast in the entire shaded region, since this is what the boundary condition assumes. In this case, boundary values of all plasma and field variables need to be set (Wu & Wang 1987). Since LFM uses an eighth order numerical scheme, its ghost region must be four cells deep. Furthermore, because both codes use staggered meshes, and the staggering is different, in general, all MHD variables have to be interpolated in the shaded region in Figure 1. We implemented the following interpolation scheme. First, all MAS variables are linearly interpolated in the radial direction, i.e.,

$$w_\mu(r_\mu^L) = q_{i,\mu}\, w_\mu(r_{i,\mu}^M) + (1 - q_{i,\mu})\, w_\mu(r_{i+1,\mu}^M), \quad (11)$$

where

$$q_{i,\mu} = \frac{r_{i+1,\mu}^M - r_\mu^L}{r_{i+1,\mu}^M - r_{i,\mu}^M};$$

w_μ marks the μth component of the vector of all the MHD variables $\boldsymbol{w} = \{\rho, \boldsymbol{V}, \boldsymbol{B}, T\}$; the superscripts "$L$" and "$M$" stand for LFM and MAS, respectively; $r_{i,\mu}^M$ is the radial location where the MAS variable w_μ is defined such that $r_{i,\mu}^M \leqslant r_\mu^L < r_{i+1,\mu}^M$. The notation in Equation (11) highlights the fact that the locations where different variables are defined depend on both the code and on the variable.

Once the different MAS variables are interpolated to the appropriate radial locations on the LFM grid, they are then bilinearly interpolated, similarly to (11), within the spherical surface to the corresponding (θ, ϕ) locations, where θ and ϕ are the polar and azimuthal angles, respectively. An additional caveat worth mentioning is that the MAS code records the ion, not the total plasma temperature, which is taken into account by setting $T^L = 2T_i^M$.

One exception to the above procedure is the radial component of the magnetic field, B_r. Since it is the magnetic field component threading the surface of the boundary, the condition $\nabla\cdot\boldsymbol{B} = 0$ requires that B_r be evolved by applying the appropriate electric field within the surface of the boundary. Figure 2 illustrates the situation. The index notation is such that $\{i, j, k\}$ indices correspond to the $\{r, \theta, \phi\}$ dimensions. The rightmost cell in the figure corresponds to the first ghost cell below the boundary interface. The face of this cell lying within the surface of the interface is colored green. The remaining three ghost cells corresponding to the same (j, k) indices are also shown. We assume that the i-indices of the ghost cells are $\{0, -1, -2, -3\}$ going inward. The LFM staggering is such that the magnetic fields are defined at the centers of the corresponding faces as indicated in the figure. The magnetic field component threading the surface of the boundary is then $B_i(1/2, j, k)$ and is determined by the curl of the corresponding electric fields (E_j, E_k), defined at cell edges lying within the boundary. The electric fields themselves are computed from the high-order interpolated values of the corresponding components of the velocity and magnetic field, whereby B_j and B_k components are interpolated along the i-direction, while B_i is interpolated along the j and k directions (see Lyon et al. 2004, for details). Therefore, only B_j and B_k fields need to be defined in the ghost cells.

Given this procedure, our coupling algorithm for $B_r(r_i, \theta, \phi, t)$ evolution consists of the interpolation of the magnetic field components B_θ and B_ϕ and all the plasma velocity components inside the ghost cells to the appropriate locations. Here, r_i is the heliocentric distance to the boundary interface. Provided that we start with the correct initial conditions for $B_r(r, \theta, \phi, t = 0)$ everywhere at $r \geqslant r_i$, this should ensure that $B_r(r_i, \theta, \phi, t)$ will evolve correctly at all later times. As shown below, this procedure does indeed work very well.

The coupling algorithm we developed is sufficiently flexible that both the coronal and heliospheric computations can be performed in either the heliographic or the rotating frame. If both computations are carried out in the same frame, then the procedure outlined above is used. If the calculations are done in different frames, then, in addition to the above procedure, the appropriate transformation is performed such that

$$V_\phi^I(r, \theta, \phi) = V_\phi^R(r, \theta, \phi) + \Omega r\sin\theta, \quad (12)$$

where the superscripts denote the inertial and rotating frames, correspondingly. Furthermore, an additional rotation in ϕ is

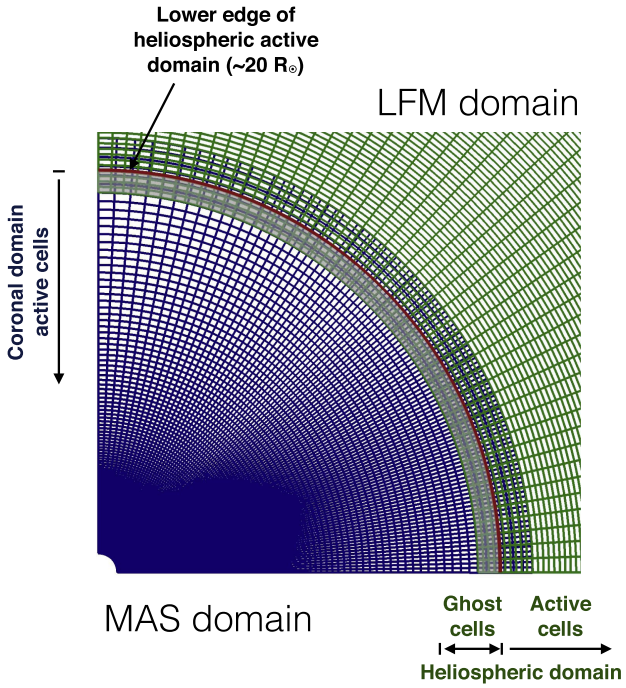

Figure 1. Schematic representation of the coupling algorithm between MAS and LFM. A 90° portion of a planar cut through the overlapping grids of the two codes is shown. The blue grid represents the coronal code active domain. The green grid represents the heliospheric code domain. The red line indicates the boundary interface, i.e., the lower boundary of the heliospheric code active domain. The shaded region represents the ghost cells of the heliospheric code.

necessary in this case, as mentioned by RL13:

$$\boldsymbol{w}^I(r, \theta, \phi, t) = \boldsymbol{w}^R(r, \theta, \phi - \Omega t, t). \quad (13)$$

The final note we make in this section is that the LFM time step is usually in the tens of seconds or smaller (dependent on resolution), while saving the MAS-c output at this time cadence is not feasible. Thus, dependent on the speed of the CME, the MAS output is saved roughly every few minutes, and the LFM boundary values are linearly interpolated in time between these states.

4. RESULTS

The results presented in this section are based on the MAS-c and MAS-h simulation runs previously performed and discussed by RL13. In different subsections below, we either use exactly the same simulations as RL13 or simulations with the same setup but with increased resolution. The LFM results are also presented at different resolutions in different subsections below. The parameters of the different runs of both MAS and LFM models presented in Sections 4.1, 4.2.1, 4.2.2, and 4.2.3 are summarized in Table 1. We will clearly identify what model runs were used when the results are presented in these sections. The time cadence of the MAS-c output files in all of the runs presented below was ≈5 minutes. Following RL13, all numerical experiments in Sections 4.1, 4.2.1, 4.2.2, and 4.2.3 were driven by the polytropic MAS-c model and used the polytropic index $\gamma = 1.05$. The more realistic CME (Section 4.2.4) was driven by the thermodynamic MAS-c and used $\gamma = 1.5$ in the heliosphere. The reader is referred to RL13 for a detailed description of the MAS-c and MAS-h simulations used herein, but we mention briefly that in all cases idealized magnetic configurations were simulated and a modified Titov & Démoulin (1999) flux-rope model (Titov et al. 2014) was employed to trigger a CME. The polytropic runs used an out-of-equilibrium flux rope, while the thermodynamic run started with a magnetically stable flux rope and triggered the eruption by flows converging to the polarity inversion line.

4.1. Testing the Coupling Interface

The results in this section are based on the simulation coronal runs performed by RL13 for the non-rotating case with an axisymmetric background solar wind. The reader is referred to Section 3.1 of that paper for details of the simulation setup. The relevant parameters of this run are summarized under MAS-c in Table 1. To maximally simplify the environment in which our numerical tests are done in this paper, the LFM code was run on a uniform spherical grid, though the use of a spatially adapted grid is a key functionality of the code. The results in this section are based on the LFM run with parameters summarized under "LFM HR" in Table 1. The angular resolution was thus similar to MAS-c but with cells distributed uniformly, while the radial resolution was substantially higher in the LFM simulation.

Figure 3 presents a combined analysis of the coupling algorithm performance during the CME passage. Each row in the figure represents one variable. A slice through both the MAS-c and LFM simulations is made near the boundary interface and at ϕ close to the center of the region of the CME passage. Then, the values of the corresponding variable are plotted as a function of the polar angle θ and time, t. It is clear from the figure that the coupling machinery performed as intended as the color plots are virtually indistinguishable. The very close agreement of the minimum/maximum values, indicated at the top of the color panels, confirms this point. To further verify the agreement between the two codes, the line plots in the last column compare the corresponding variables at a fixed θ as a function of time. These plots reveal an interesting detail: while all other variables line up nearly exactly between the two codes, B_r in the LFM solution, while also nearly identical to the MAS-c result, may be shifted by a few minutes. This shift is not constant in time but is always comparable to or less than the MAS-c input cadence. We further analyze the $B_r(r_i, \theta, \phi, t)$ evolution at the LFM inner boundary ($r = r_i$) below, but mention here one plausible reason for the weak deviation of the LFM result from MAS-c. We mentioned above that in the coupling algorithm currently implemented, all variables, except B_r, are linearly interpolated in time between the MAS-c updates (~5 minutes). By construction, this guarantees that the time-interpolated variables will take the same values as in MAS-c (spatial interpolation aside) and will not deviate significantly between the updates as long as the update cadence is sufficiently fine, i.e., $t_n - t_{n-1} \ll w/|\partial w/\partial t|$, where w is the interpolated variable. However, B_r, is evolved in time by the LFM code self-consistently from the initial state by applying the corresponding B_θ, B_ϕ, and $\boldsymbol{v}$ in the ghost region, and is not forced to be the same as in the MAS-c code. Keeping this in mind, the consistency of $B_r(r_i, \theta, \phi, t)$ in LFM and MAS-c solutions (Figures 3(m)–(o)), including the temporal evolution, is rather remarkable. We note that, in principle, other methods of temporal interpolation for B_r evolution can be used (RL13, Merkin et al. 2016) that would ensure that $B_r^L(r_i, \theta, \phi, t_n) = B_r^M(r_i, \theta, \phi, t_n)$, where t_n are the times of MAS-c updates, and L and M superscripts stand for LFM and MAS, as before. Given the good performance of the currently

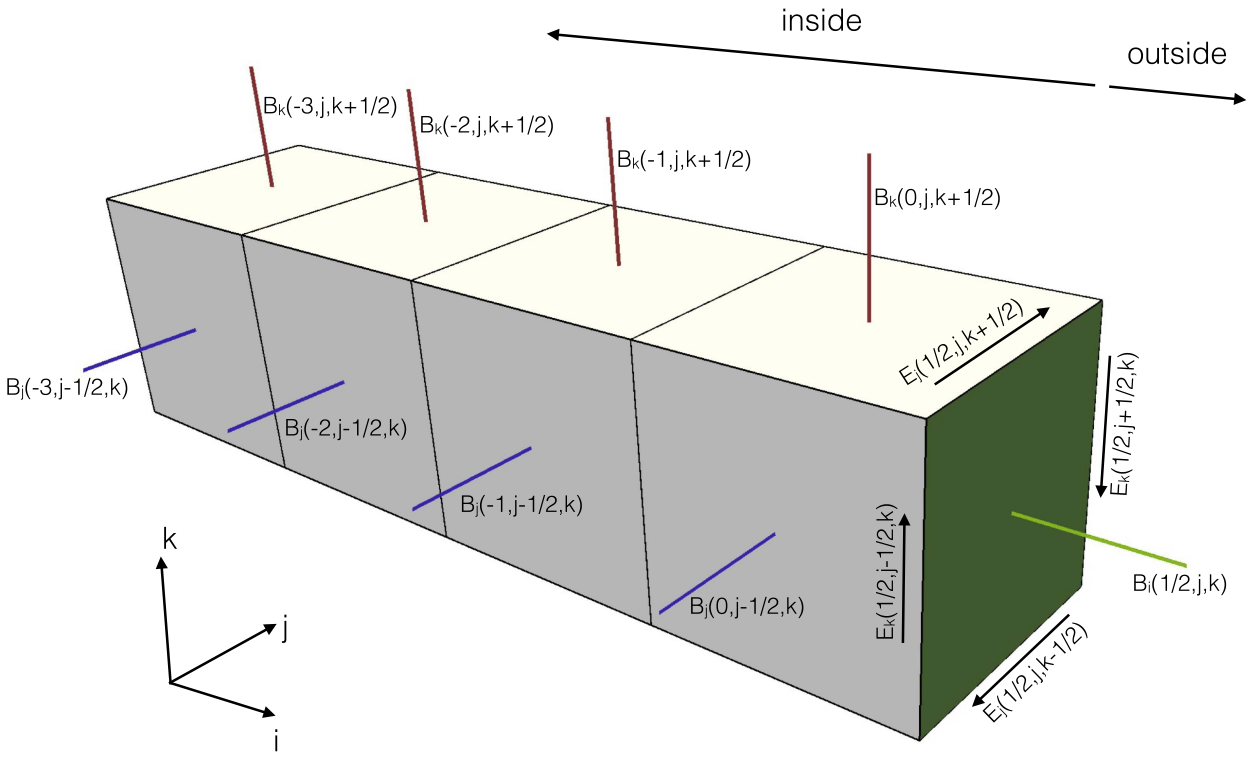

Figure 2. Schematic representation of LFM-helio ghost region below its lower boundary. The green cell face lies within the boundary interface as defined above (see Figure 1). The locations of the staggered electric and magnetic field components are indicated. The $\{i, j, k\}$ indices correspond to $\{r, \theta, \phi\}$ dimensions.

Table 1
Model Run Parameters Used in Sections 4.1, 4.2.1, 4.2.2, and 4.2.3

	MAS-c[a]	MAS-h LR[a]	MAS-h HR	LFM LR	LFM HR
Number of cells, $N_r \times N_\theta \times N_\phi$	200 × 150 × 200	46 × 150 × 200	600 × 300 × 400	106 × 96 × 128	212 × 256 × 512
Resolution	variable, ∼0.°5 × 0.°5[b], $d_r \approx 0.5$[c,d]	variable, ∼0.°5 × 0.°5[b], $0.5 \lesssim d_r \lesssim 0.9$	×2 angular, uniform radial, $d_r \approx 0.05$	uniform, ∼1.°9 × 2.°8, $d_r \approx 0.3$	uniform, ∼0.°7 × 0.°7, $d_r \approx 0.14$
Radial extent	1–50	20–50	20–50	20–50	20–50

Notes.
[a] Runs presented by RL13.
[b] In the region of CME propagation.
[c] At the boundary interface.
[d] Units of distance are $R_\odot$.

implemented algorithm, we have opted for its use in this paper, but may implement a more accurate method in the future.

In Figure 4, we further explore the time evolution of the radial magnetic field, B_r, at the boundary interface between MAS-c and LFM. Panels (a)–(c), (d)–(f), and (g)–(i) correspond to three instances of time prior to the CME passage through the boundary, during it, and near the end of the simulation. The panels depicting 3D visualizations compare the spatial distribution of the MAS-c (a), (d), (g) and LFM (b), (e), (h) solutions at different times. It is clear from these 3D visualizations that the solutions for B_r in both codes are very similar in terms of their spatial distribution as well as their temporal evolution. Quantitatively, this is confirmed by the minimum/maximum values indicated in the bottom right corner of the corresponding panels. To further verify this visual impression, we make a meridional slice through the simulation indicated with the black line in the 3D visualizations and plot the resulting comparisons in panels (c), (f), and (i). Clearly, the differences between the two codes are minor. Initially, the primary difference is due to the spatial interpolation of the sharp $\partial B_r/\partial\theta$ gradient at the current sheet. As time progresses, the deviations may become larger (e.g., panel (i)), but according to the minimum/maximum values, they remain within 2%–3%.

4.2. Heliospheric Solutions

Now that we have established the proper functioning of the coupling interface, we can go ahead and validate the resulting heliospheric solutions of the MAS and LFM codes against each other. We first compare the initial background solutions for the non-rotating case discussed above (Section 4.2.1). We then compare the solutions for the same case after the passage of the CME through the boundary and explore the effects of the spatial resolution of our simulations (Section 4.2.2). Section 4.2.3 then shows comparisons of MAS-h and LFM

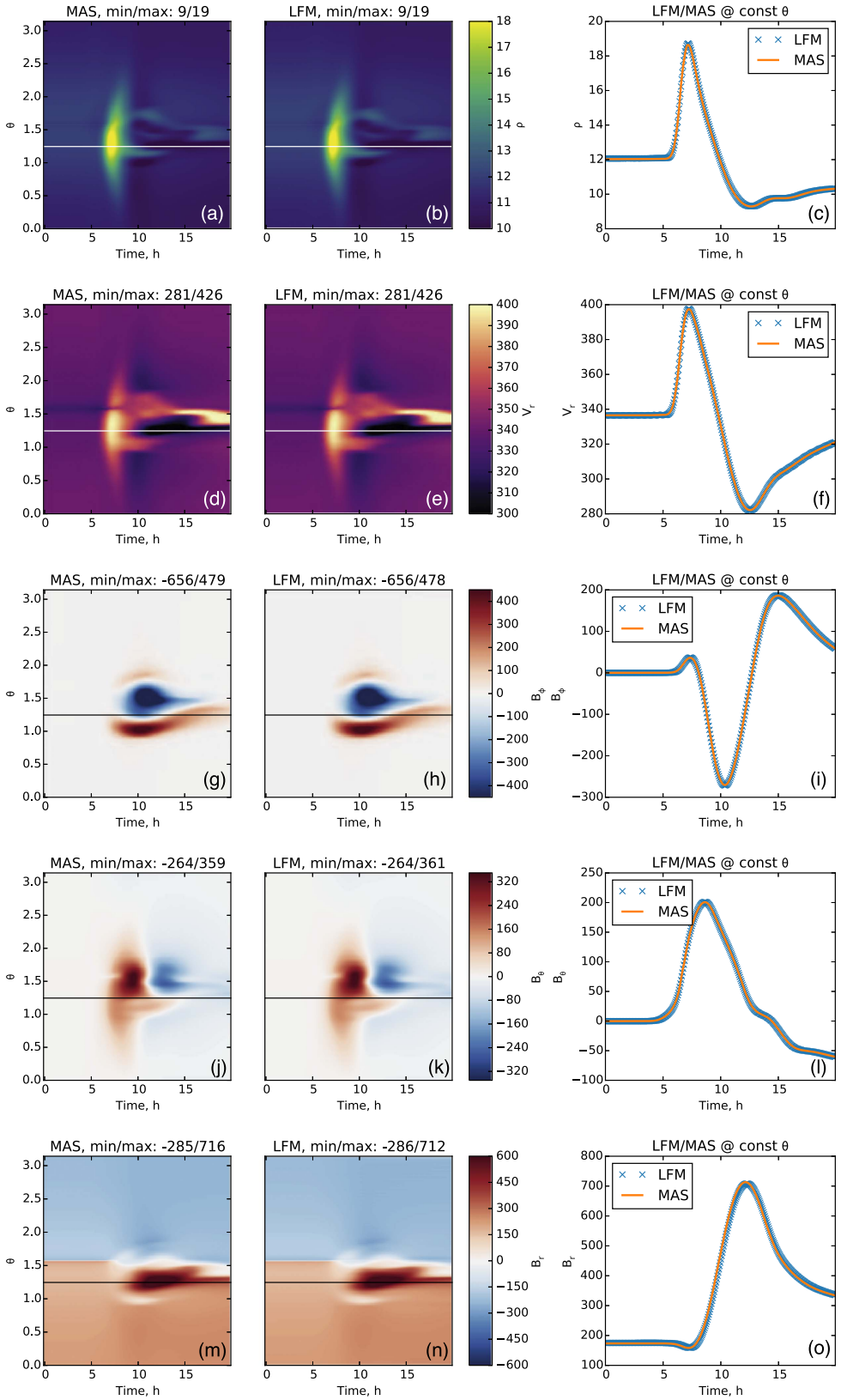

Figure 3. Test of the boundary interface between the MAS-c and LFM codes for the non-rotating case. A meridional slice through both simulations is taken at the center of the first active LFM cell above the boundary interface ($r \approx 20.7\ R_\odot$) and $\phi \approx 87°$ (i.e., nearly the $x = 0$ plane), roughly in the middle of the region where the CME flux rope is passing through the interface. Each row corresponds to one variable: (a)–(c) ρ [cm^{-3} $\times$ 10^{-3}], (d)–(f) V_r [km s^{-1}], (g)–(i) B_ϕ [nT], (j)–(l) B_θ [nT], (m)–(o) B_r [nT]. The plots in the left and middle columns represent the corresponding variable as a function of the polar angle θ and time. The right column shows the comparison along the slice at $\theta \approx 71°6$ indicated in the plots in the left and middle columns with the horizontal line. The min/max values are indicated at the top of the plots in the left and middle columns.

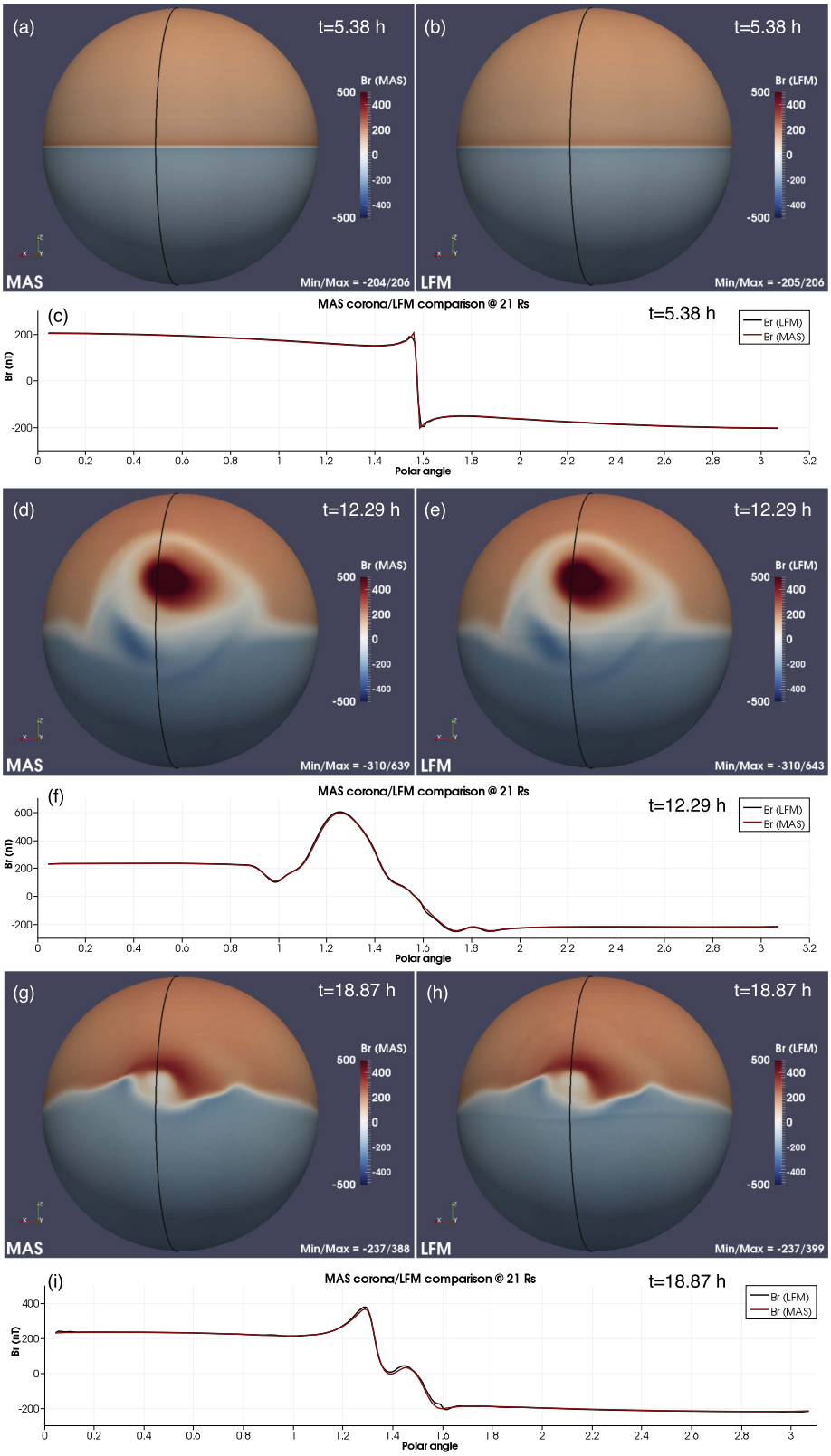

Figure 4. Time evolution of the radial magnetic field, B_r, in the MAS-c and LFM codes just above the boundary interface ($r = 21\ R_{\odot}$) for the non-rotating case. The solutions are shown for three time instances: just prior to the CME passage at $t = 5.38$ hr (a)–(c), during the CME passage at $t = 12.29$ hr (d)–(f), and toward the end of the simulations $t = 18.87$ hr (g)–(i), compare to Figure 3. In the 3D color plots, MAS results are shown in the left column (a), (c), and (g), while LFM results are on the right (b), (e), and (h). The line plots compare the two codes along the meridional slice near the $x = 0$ plane, indicated by the black trace in the color plots. The orientation axes of the 3D view are shown in the lower left corner of the color plots, while min/max values are indicated on the lower right. Units are nT.

solutions for a rotating CME case in a similar axisymmetric background. Finally, Section 4.2.4 describes a more realistic rotating case with an asymmetric background.

4.2.1. Background Solutions

In the previous section, we established that the values near the LFM coronal boundary evolve in agreement with the MAS-c values inserted into LFM as the boundary condition. In other words, we have established that the boundary interface works as intended. It is now equally important to establish that the initial condition for the subsequent CME propagation—throughout the simulation domain—is correct. We do this using the same non-rotating axisymmetric background case as discussed in the previous section. The model run parameters are "MAS-h LR" and "LFM HR" (Table 1).

Figure 5 shows the solutions for the scaled radial magnetic field ($\times(r/r_i)^2$) (a)–(c), plasma speed (d)–(f), and scaled density (g)–(i). Panels (a)–(b), (d)–(e), and (g)–(h) compare the MAS-h and LFM solutions in the volume of the simulation, while panels (c), (f), and (i) show the comparisons near the outer boundary ($r = 48\,R_\odot$) in the meridional plane. While the 3D visualizations indicate nearly identical solutions (corroborated, again, by the min/max values in the lower right corner), the line plots reveal small differences between the solutions. The primary differences in the magnetic field (panel (c)) are near the current sheet, but those existed near the inner boundary already (see Figure 4). Thus, this indicates that the current sheet did not diffuse significantly in either of the codes as the simulations progressed. The differences in the plasma speed and density (panels (f) and (i)) are only apparent because the line plots were intentionally zoomed in. These differences are on the order of 1% or smaller and only emphasize the strong agreement between the two simulations.

4.2.2. Non-rotating, Axisymmetric Background Case

Having established both the proper functioning of our boundary interface and the correct steady-state background heliospheric configurations, we now turn our attention to the comparison of LFM and MAS-h solutions during the transient stage of the CME propagation. We select one time instance close to the end of the simulation ($t \approx 20$ hr) when the front edge of the CME is approaching the outer boundary ($r = 50\,R_\odot$). For the results presented in this section, we performed two additional simulations: one significantly increased the resolution of the MAS-h model ($\times 2$ for the angular dimensions and ~10–20-fold for the radial dimension; see "MAS-h HR" in Table 1). For the LFM code, in contrast, the additional run had a lower resolution than "LFM HR" discussed heretofore (see "LFM LR" in Table 1). In this and the subsequent Section (4.2.3), we only show the comparisons of the V_r, B_θ, and B_ϕ variables to avoid cluttering the presentation. The comparisons in the remaining variables are similar and do not provide any additional information.

Figures 6–8 depict 3D visualizations of V_r, B_θ, and B_ϕ, respectively. Panels (a)–(b) depict the results of the lower resolution simulation runs ("MAS-h LR" and "LFM LR" in Table 1), while panels (c)–(d) show the results for higher resolution ("MAS-h HR" and "LFM HR" in Table 1). No substantial differences between either of the four runs are evident in the morphology of the V_r solutions, but closer examination reveals a somewhat stronger flow in the "LFM LR" run in the low-speed region seen in the meridional plane (Figure 6(b)) and also a somewhat stronger flow in the equatorial region in the "MAS-h LR" simulation (Figure 6(a)). This is confirmed by the line plot (Figures 6(e)) comparing the four simulation runs along the $r = 34\,R_\odot$ circle in the meridional plane marked with the black trace in Figures 6(a)–(d). The line plot indicates almost identical solutions in the "MAS-h HR" and "LFM HR" simulations with weak deviations in the "MAS-h LR" and "LFM LR" runs. While these deviations are small in relative terms (~3%), the subsequent figures (Figures 7–8) reveal much more marked differences between the lower and higher resolution MAS-h runs, while the differences introduced by the change in the LFM resolution are rather minor. Note that the line plots in Figures 7(e) and 8(e) are made at different radial distances (34 and $36\,R_\odot$, respectively) to ensure that they trace the large amplitude regions in the corresponding field components. In particular, for the most geoeffective B_θ magnetic field component (Figure 7), as well as the B_ϕ component (Figure 8), the min/max values in the LFM solutions change by a few nT. In contrast, the higher resolution MAS-h (Figures 7(c) and 8(c)) produced B_θ nearly twice as strong as the lower resolution MAS-h (see Figure 7(b)) and the minimum B_ϕ value stronger by 25% (see Figure 8(b)). The line plots in Figures 7(e) and 8(e) confirm the significant deviation of the "MAS LR" run from the other runs, while demonstrating the weak dependence of the LFM runs on the resolution.

We also performed an additional MAS-h run at an intermediate resolution: it had the same angular resolution as "MAS-h HR" but with the radial resolution doubled with respect to "MAS-h LR" (i.e., ranging between ~0.25 and $0.45\,R_\odot$ for $20 \leqslant r \leqslant 50\ R_\odot$). The radial resolution of that simulation was thus roughly the same as the "LFM LR" resolution on average: finer at smaller r and coarser at larger r. The results from that run (not shown) were somewhere in between the "MAS-h LR" and "MAS-h HR" runs thus indicating the progressive convergence of the MAS-h solutions with increasing resolution. The LFM solutions are evidently already sufficiently resolved at the lower resolution, though the differences between "LFM LR" and "LFM HR" are not negligible (e.g., Figure 6). Figures 6–8 generally confirm the same picture: "MAS-h HR" is hardly distinguishable from either "LFM LR" or "LFM HR," while "MAS-h LR" is clearly under resolved.

4.2.3. Rotating, Axisymmetric Background Case

The results discussed heretofore have been obtained from simulations with no solar rotation included. In this section, we relax this limitation. Both the LFM simulations and the MAS-c simulation driving them were performed in the rotating frame, while the MAS-h simulations, with which LFM is compared were carried out in the inertial frame (see Section 3.2 in RL13). Figures 9–11 present the comparisons in the same format as Figures 6–8 in the previous section. Compared to the previous section, however, the meridional plane was rotated by $\Delta\phi \approx -11^\circ$ to capture the CME from roughly the same perspective, accounting for the solar rotation over the 20 hr of the simulation. Solar rotation is evidenced, in particular, by the presence of the weak B_ϕ at the inner boundary ($r = 21\,R_\odot$) of the simulations in all panels of Figure 11.

As in the preceding section, the differences in the V_r distribution (Figure 9) are relatively minor with "MAS-h LR"

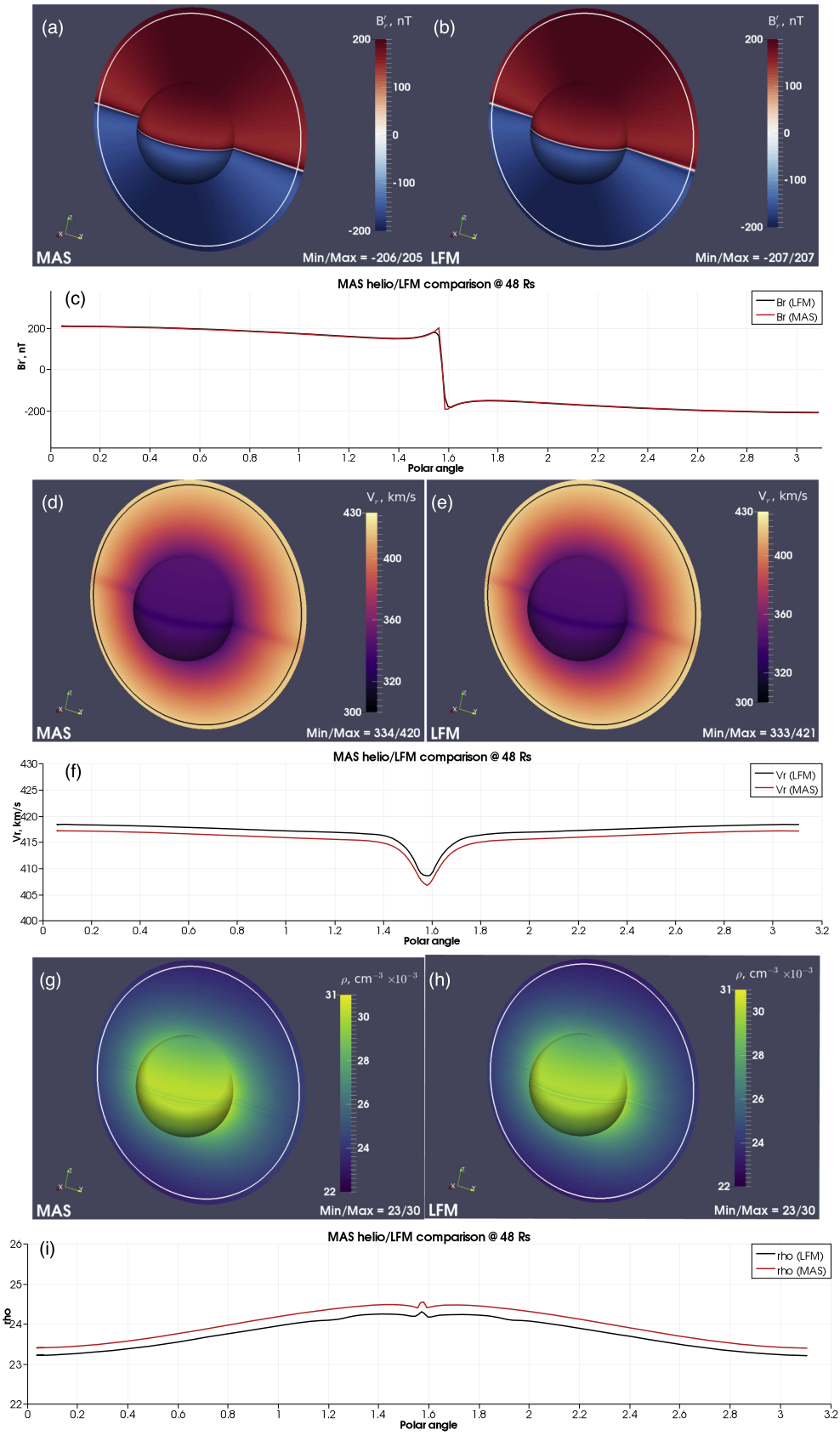

Figure 5. Comparison of the background MAS-h and LFM solutions for the non-rotating case. A meridional plane at $x \approx 0$ and the spherical surface near the LFM inner boundary ($r \approx r_i$, $r_i = 21\ R_\odot$) are color coded as follows: radial magnetic field component scaled as r^2, $B'_r = B_r(r/r_i)^2$ in MAS-h (a) and in LFM (b); plasma speed in MAS-h (c) and LFM (d); plasma density in MAS-h (g) and LFM (h). The line plots (c), (f), and (i) show the corresponding variables in the meridional plane at $r = 48\ R_\odot$ as a function of the polar angle θ. The 48 $R_\odot$ surface is indicated by the white (a), (b), (g), (h) or black (d), (e) circular trace in the meridional plane in all color plots. The orientation axes of the 3D view are shown in the lower left corner of the color plots, while min/max values are indicated on the lower right.

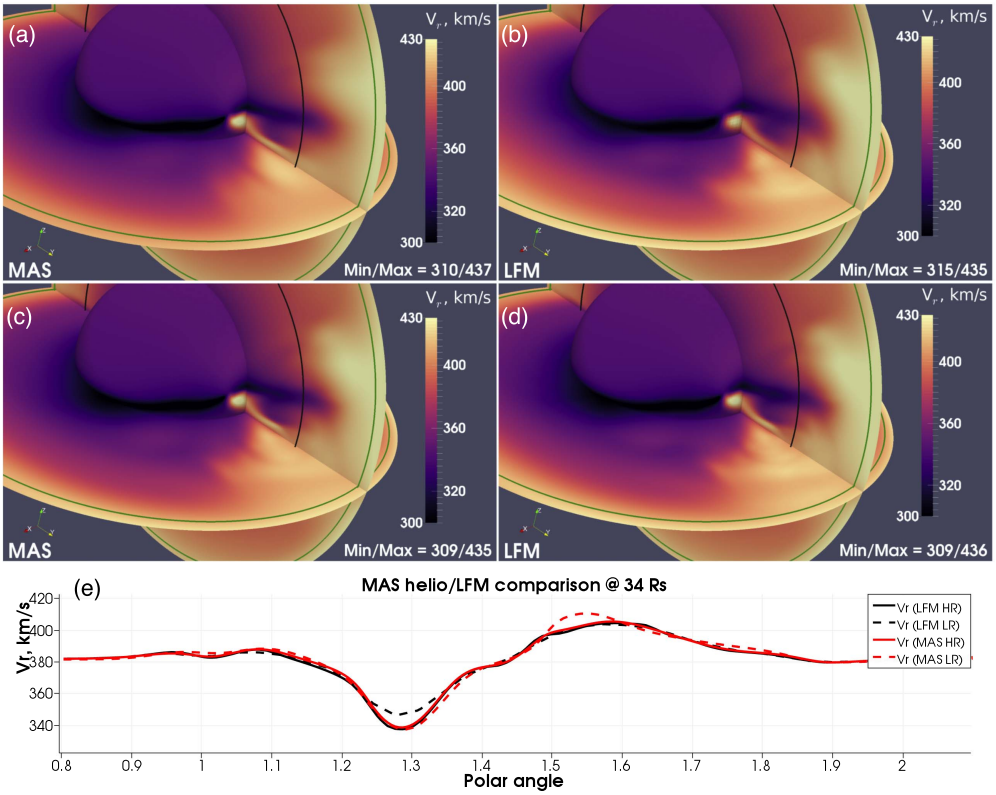

Figure 6. Comparison of V_r in (a) MAS-h and (b) LFM at low resolution ("MAS-h LR" and "LFM LR" in Table 1) for the non-rotating case at simulation time $t \approx 20$ hr. (c–d) The same for high resolution ("MAS-h HR" and "LFM HR" in Table 1). In panels (a)–(d), three slices through the 3D volume of the simulation are shown: radial slice at $r = 21\ R_\odot$, meridional slice at $x = 0$, and equatorial slice at $z = 0$. The orientation axes are shown in the lower left corner. Min/max values in the meridional plane are indicated in the lower right corner. The circular traces in the meridional plane indicate the $r = 34\ R_\odot$ (black) and $r = 48\ R_\odot$ (green) spherical surfaces. The latter is additionally shown in the equatorial plane. Panel (e) shows the comparison along the $r = 48\ R_\odot$ meridional trace for all four models as marked in the legend. Note the range of the horizontal axis in panel (e) has been intentionally zoomed in to emphasize the region where the differences between the codes are most pronounced.

and "LFM LR" runs deviating by a comparable amount from the corresponding high-resolution runs. However, the B_θ and B_ϕ distributions (Figures 10 and 11) show essentially the same picture as for the non-rotating case: the LFM results are only weakly dependent on the simulation resolution while the MAS-h results exhibit significant changes; at the high resolution, the MAS results become much closer to the LFM simulation. In particular, the B_θ maximum value nearly doubles in strength at the higher MAS-h resolution (Figure 10(a) versus Figure 10(c); see also Figure 10(e)). Marked differences are also apparent in Figure 11(a) versus Figure 11(c) (see also Figure 11(e)), while the latter is quite consistent with the LFM result in Figures 11(b) and (d). Note that the similarity between Figures 6–8 and 9–11, correspondingly, additionally confirms the correct performance of the coupled simulation when solar rotation is included.

4.2.4. A More Realistic Case

Encouraged by the success of the more simple experiments presented in the previous sections of the paper, we have run a more realistic interplanetary CME simulation, which is discussed in Section 4 of RL13 and, in somewhat more detail, in Schwadron et al. (2014, 2015). Unlike the previous simulations, which were driven by the polytropic MAS-c code and used $\gamma = 1.05$, here the LFM heliospheric simulations were driven by the thermodynamic MAS-c code, and $\gamma = 1.5$ was set, which is a more realistic value for the solar wind in the inner heliosphere (Totten et al. 1995). For this CME simulation, the MAS-c calculation was carried out in the rotating frame, but without including the fictitious forces. The LFM heliospheric simulation was performed in the inertial frame, the MAS-c grid was assumed to be rotating underneath with the angular rate $\Omega = 2\pi/25.38$ day, and, additionally, a corotation component of the azimuthal magnetic field was included, $B_\phi^{\rm rot} = -\Omega r \sin\theta / V_r$. Because of the computational constraints of the thermodynamic MAS-c model the MAS-c coronal simulation was used to drive the inner boundary of the LFM heliospheric simulation for 20 hr, as in RL13, which was sufficient for the CME flux-rope structure to propagate through the boundary interface between the codes. After this 20 hr period, the last frame of the MAS-c simulation was used for the remainder of the run as a corotating boundary condition. Unlike the more simple tests above, here the simulation domain extended from 18 $R_\odot$ to the Earth's orbit at 1 au. The MAS-c simulation had the angular resolution of $N_\theta \times N_\phi = 300 \times 260$ at the boundary interface with LFM ($r = 18\ R_\odot$), which was highly non-uniform and provided cell sizes as small as $d_r \times d_\theta \times d_\phi \approx 0.2\ R_\odot \times 0.^\circ 1 \times 0.^\circ 1$ in the region of the CME propagation. The LFM grid was uniform spherical with the size of $N_r \times N_\theta \times N_\phi = 384 \times 192 \times 384$.

Figure 12 shows three snapshots of the simulation: (a) just prior to the CME passage through the boundary between the models, (b) after the passage, and (c) roughly midway en route to the Earth's orbit. As can be seen from the structure of the magnetic field lines as well as the plasma streams, the background is both

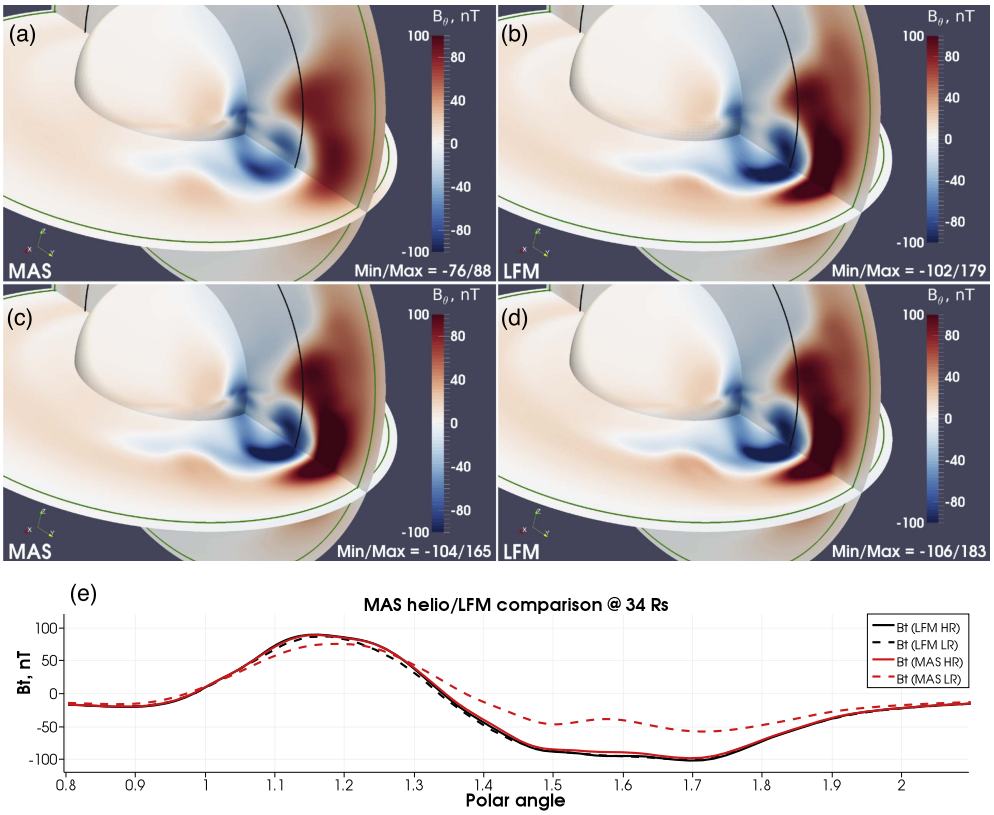

Figure 7. Same as Figure 6, but for B_θ.

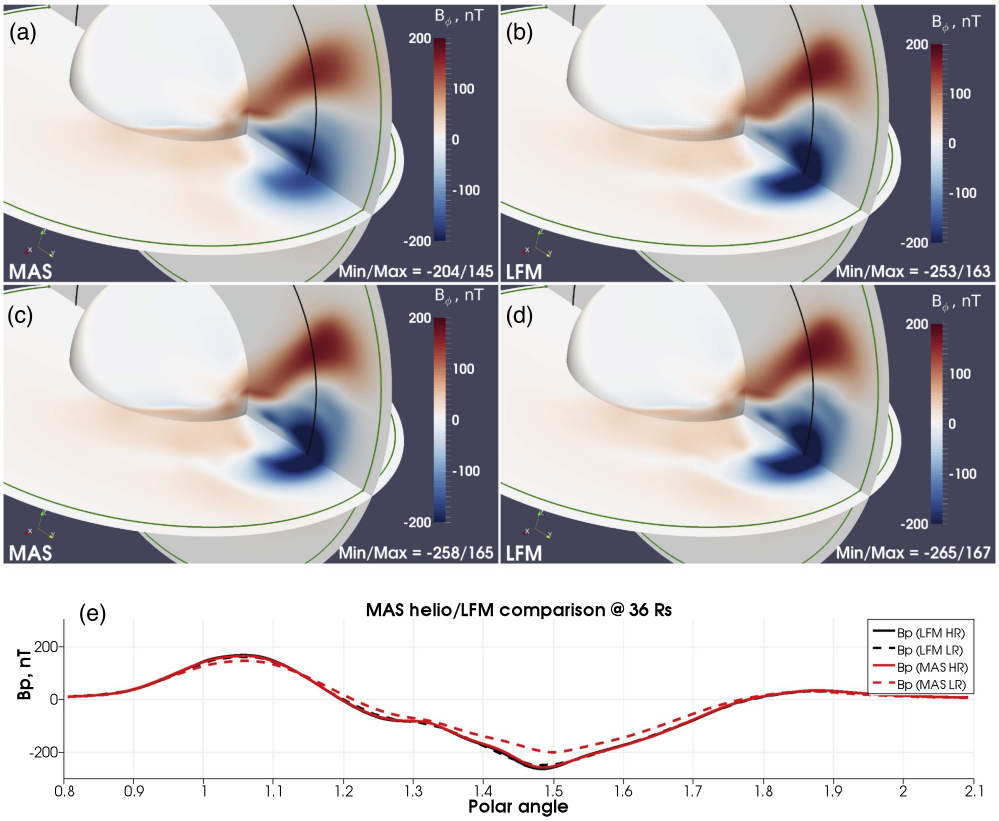

Figure 8. Same as Figure 6, but for B_ϕ. Note that, unlike in Figures 6 and 7, the meridional trace (black trace in panels (a)–(d)) is placed at $r = 36\ R_\odot$ as panel (e) indicates.

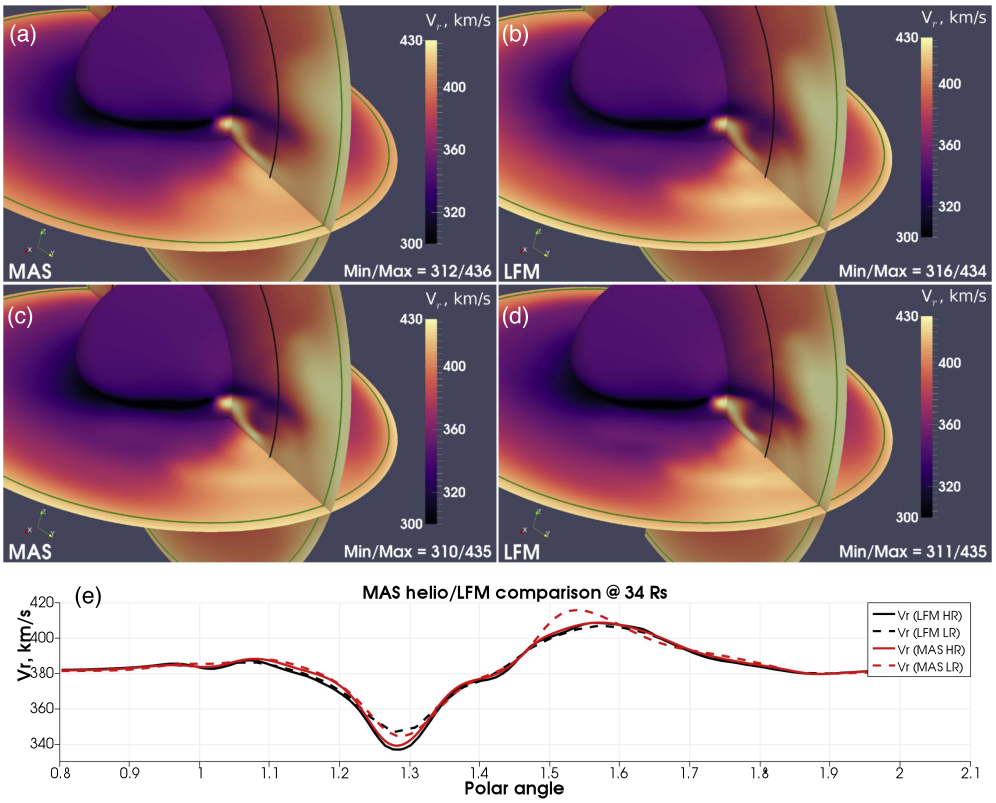

Figure 9. Same as Figure 6, but for the rotating case. Also, relative to Figure 6, the meridional plane is rotated by approximately −11°. See the text for details.

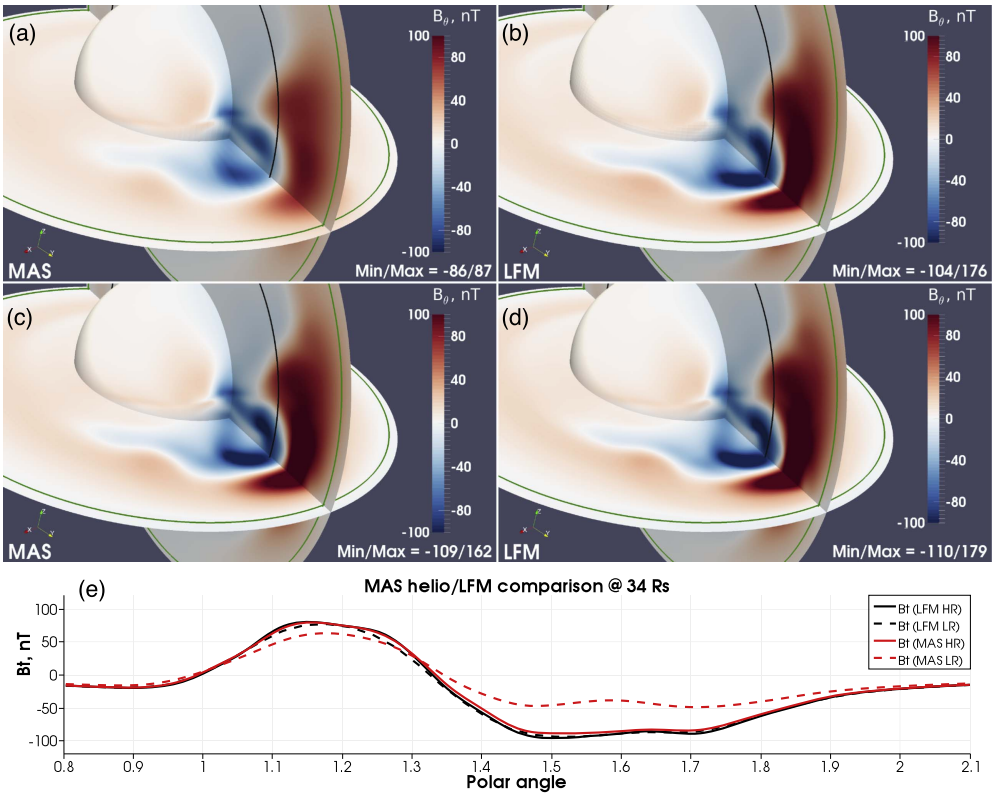

Figure 10. Same as Figure 7, but for the rotating case. Also, relative to Figure 7, the meridional plane is rotated by approximately −11°. See the text for details.

azimuthally asymmetric and includes the solar rotation. The strong plasma speed gradients are well-captured by the LFM code, and a significant geoeffective magnetic field component B_z persists throughout the simulation. In particular, the part of the flux rope farthest from the observer indicates negative B_z values (green color) in excess of −15 nT, e.g., in Figure 12(c). The high-

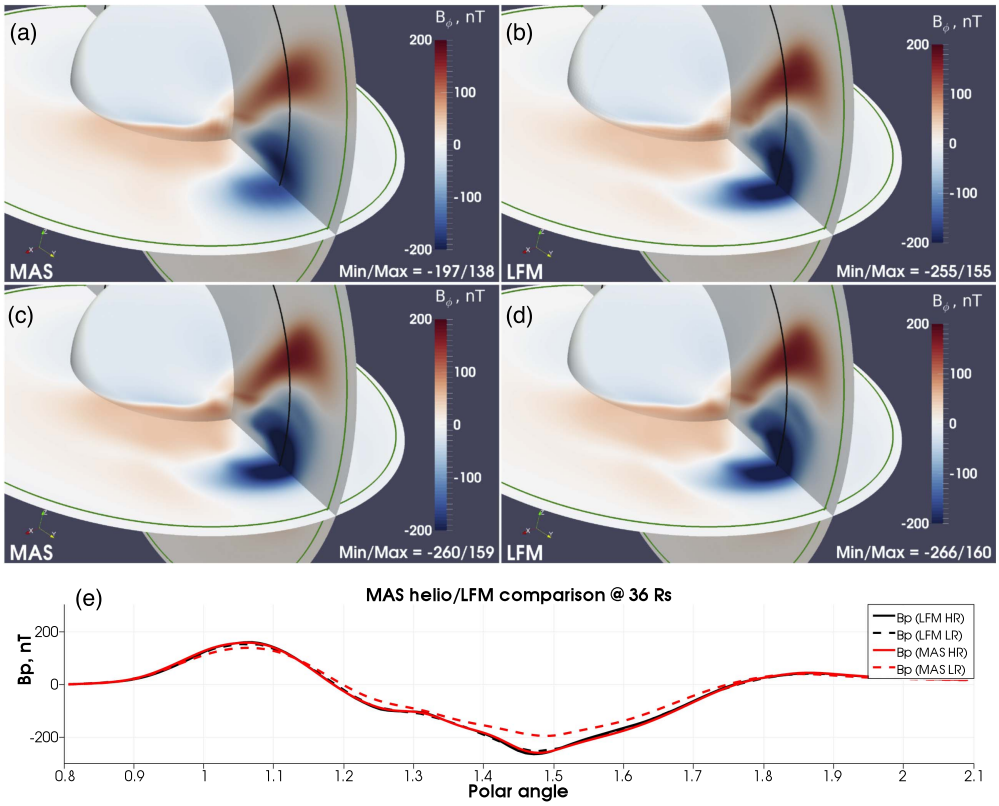

Figure 11. Same as Figure 8, but for the rotating case. Also, relative to Figure 8, the meridional plane is rotated by approximately −11°. See the text for details.

speed streams in the wake of the CME are associated with relatively narrow, but pronounced density depletions. Those are most likely a result of magnetic reconnection, and lead to a localized increase of the Alfvén speed and, thus, to larger flow speeds. Similar post-eruptive reconnection-driven outflows have been reported previously in MHD simulations and were found to be consistent with observations (Riley et al. 2002). The duration of these streams is also possibly artificially increased due to the fixed corotating boundary condition following 20 hr of time-dependent driving.

The purpose of this section was to demonstrate the proper functioning of our coupling interface and the ability of the coupled MAS–LFM model to simulate a more realistic CME propagation throughout the inner heliosphere. The simulation itself is sufficiently sophisticated, and the results are sufficiently complex, that we defer a more detailed analysis to a dedicated publication.

5. SUMMARY AND CONCLUSIONS

This paper describes an effort to develop and verify a coupled model of the solar corona and the inner heliosphere. The MAS model was used to simulate CME initiation and dynamics in the corona. The output from the coronal MAS was then used to drive the LFM model of the inner heliosphere. We presented a number of numerical tests including non-rotating and rotating CMEs in the axisymmetric background, as well as a more realistic CME simulation with both rotation and asymmetric background. We demonstrated the correct performance of the boundary interface between the models and verified the heliospheric results by comparing heliospheric MAS and LFM solutions at different grid resolution. While the initial background conditions were reproduced nearly identically by both codes, the time-dependent behavior of the CME in the heliosphere exhibited dependence on the model resolution. When run at progressively finer resolution, the heliospheric MAS solutions gradually approached the LFM results, while the latter showed only a weak dependence on the resolution.

In this paper, we were concerned with the development and verification of the coupling infrastructure between our coronal and heliospheric models. Our focus has been on testing the coupling interface and explaining the differences between the different heliospheric solutions rather than on in depth analysis of the simulated heliospheric structures. Such applications to problems of CME propagation in the inner heliosphere are enabled now that we have gained confidence in the fidelity of the coupled model.

The results presented above have significant implications for such studies. The large and rapidly growing body of work on MHD modeling of interplanetary CMEs lends importance to the notion that the numerical solutions may be subject to the dependence on the mesh resolution—as shown herein—or possibly to other details of model numerics. Thus, caution must be exercised in the interpretation of model results for establishing the true system behavior. Even though there are indications that CME propagation is not a chaotic process (Pizzo et al. 2015), our results suggest that variability in solutions between different models may necessitate ensemble modeling based not only on paramet.er variation within one model but on ensembles of different models as well.

Ultimately, understanding of the true system behavior cannot be gained without observations. Most promising are comparisons of models with heliospheric imaging (e.g., Odstrcil & Pizzo 2009; Lugaz & Roussev 2011), but these are not conclusive because of uncertainties in observations themselves. Simulations, on the other hand, can be helpful in interpreting

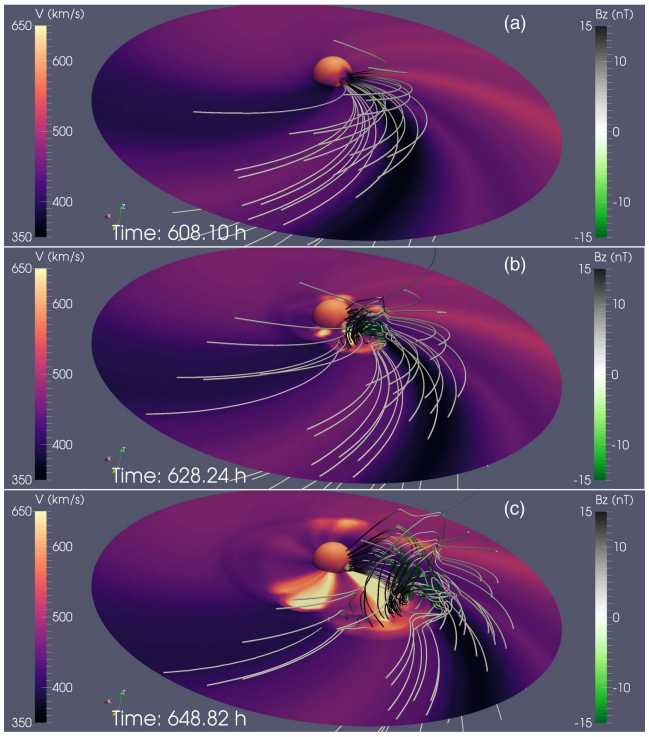

Figure 12. Realistic CME simulation in the interplanetary space. The equatorial slice and the spherical slice near the LFM inner boundary $r = 18\ R_{\odot}$ are color coded with the plasma speed. A number of magnetic field lines are traced from fluid elements starting near the inner boundary of the simulation and moving with the plasma. The field lines are color coded by the B_z magnetic field component. The panels in the figure depict the simulation just prior to the CME passage through the boundary (a), after the passage (b), and midway en route to 1 au (c).

the observations (Aschwanden et al. 2006), but this requires a high level of confidence in the simulation results. Thus, it is only by thorough model–model and model–data analysis that progress will be achieved.

This work was supported by the collaborative NSF grants AGS-1260358, AGS-1259407, and AGS-1260388. V.G.M. and J.G.L also acknowledge the NASA grant NNX13AG15G. PSI personnel were also supported by the NASA LWS Flux rope team (NASA contract NNH14CK98C), by AFOSR contract FA9550-15-C-0001, and by the NSF Frontiers in Earth System Dynamics project. We would like to acknowledge high-performance computing support from NSF-sponsored Yellowstone (ark:/85065/d7wd3xhc) provided by NCAR's Computational and Information Systems Laboratory, from NSF-sponsored Texas Advanced Computing Center (TACC), and from the NASA High-End Computing (HEC) Program through the NASA Advanced Supercomputing (NAS) Division at Ames Research Center.

REFERENCES

Aschwanden, M. J., Burlaga, L. F., Kaiser, M. L., et al. 2006, SSRv, 136, 565
Detman, T. R., Dryer, M., Yeh, T., et al. 1991, JGR, 96, 9531
Dryer, M., Detman, T. R., Wu, S. T., & Han, S. M. 1989, AdSpR, 9, 75
Forbes, T. G., Linker, J. A., Chen, J., et al. 2006, SSRv, 123, 251
Gopalswamy, N. 2006, JApA, 27, 243
Gopalswamy, N., Yashiro, S., Michalek, G., et al. 2009, EP&S, 104, 295
Gosling, J. T., Bame, S. J., McComas, D. J., & Phillips, J. L. 1990, GeoRL, 17, 901
Gosling, J. T., Hildner, E., MacQueen, R. M., et al. 1974, JGR, 79, 4581
Groth, C. P. T., de Zeeuw, D. L., Gombosi, T. I., & Powell, K. G. 2000, JGR, 105, 25053
Jacobs, C., & Poedts, S. 2011, JASTP, 73, 1148
Kataoka, R., Ebisuzaki, T., Kusano, K., et al. 2009, JGR, 114, 10102
Lee, C. O., Arge, C. N., Odstrcil, D., et al. 2013, SoPh, 285, 349
Linker, J. A., Mikić, Z., Biesecker, D. A., et al. 1999, JGR, 104, 9809
Linker, J. A., Mikić, Z., Lionello, R., et al. 2003, PhPl, 10, 1971
Lionello, R., Downs, C., Linker, J. A., et al. 2013, ApJ, 777, 76
Lionello, R., Linker, J. A., & Mikić, Z. 2009, ApJ, 690, 902
Lionello, R., Mikić, Z., & Linker, J. A. 1999, JCoPh, 152, 346
Lionello, R., Mikić, Z., & Schnack, D. D. 1998, JCoPh, 140, 172
Lugaz, N., & Farrugia, C. J. 2014, GeoRL, 41, 769
Lugaz, N., Manchester, W. B. I., & Gombosi, T. I. 2005, ApJ, 627, 1019
Lugaz, N., Manchester, W. B. I., Roussev, I. I., Toth, G., & Gombosi, T. I. 2007, ApJ, 659, 788
Lugaz, N., Manchester, W. B., IV, Roussev, I. I., & Gombosi, T. I. 2008, JASTP, 70, 598
Lugaz, N., & Roussev, I. 2011, JASTP, 73, 1187
Lugaz, N., Vourlidas, A., Roussev, I. I., & Morgan, H. 2009, SoPh, 256, 269
Luhmann, J. G., Solomon, S. C., Linker, J. A., et al. 2004, JASTP, 66, 1243
Lyon, J. G., Fedder, J. A., & Mobarry, C. M. 2004, JASTP, 66, 1333
Manchester, W. B., Gombosi, T. I., Roussev, I., et al. 2004a, JGR, 109, A01102
Manchester, W. B., Gombosi, T. I., Roussev, I., et al. 2004b, JGR, 109, A02107
Merkin, V. G., Lyon, J. G., Lario, D., Arge, C. N., & Henney, C. J. 2016, JGR, 121, 2866
Merkin, V. G., Lyon, J. G., McGregor, S. L., & Pahud, D. M. 2011, GeoRL, 38, L14107
Merkin, V. G., Sitnov, M. I., & Lyon, J. G. 2015, JGR, 120, 1993
Mikić, Z., Linker, J. A., Schnack, D. D., Lionello, R., & Tarditi, A. 1999, PhPl, 6, 2217
Odstrcil, D., Linker, J. A., Lionello, R., et al. 2002a, in The 10th European Solar Physics Meeting, Solar variability: from Core to Outer Frontiers, ed. A. Wilson (Noordwijk: ESA Publications), 95
Odstrcil, D., Linker, J. A., Lionello, R., et al. 2002b, JGR, 107, 1493
Odstrcil, D., & Pizzo, V. J. 1999, JGR, 104, 28225
Odstrcil, D., & Pizzo, V. J. 2009, SoPh, 259, 297
Odstrcil, D., Pizzo, V. J., Linker, J. A., et al. 2004a, JASTP, 66, 1311
Odstrcil, D., Riley, P., & Zhao, X. P. 2004b, JGR, 109, A02116
Pahud, D. M., Merkin, V. G., Arge, C. N., Hughes, W. J., & McGregor, S. 2012, JASTP, 83, 32
Pizzo, V. J., de Koning, C., Cash, M., et al. 2015, SpWea, 13, 676
Reames, D. V. 1999, SSRv, 90, 413
Reames, D. V. 2013, SSRv, 175, 53
Richardson, I. G., Cliver, E. W., & Cane, H. V. 2001, GeoRL, 28, 2569
Riley, P., Linker, J. A., Mikić, Z., et al. 2002, ApJ, 578, 972
Rouillard, A. P., Odstrcil, D., Sheeley, N. R., et al. 2011, ApJ, 735, 7
Schwadron, N., Lee, M., Gorby, M., et al. 2015, ApJ, 810, 97
Schwadron, N. A., Gorby, M., Török, T., et al. 2014, SpWea, 12, 323
Shen, F., Feng, X., Wu, S. T., & Xiang, C. 2007, JGR, 112, a06109
Shen, F., Feng, X. S., Wang, Y., et al. 2011, JGR, 116, A09103
Shen, F., Shen, C., Wang, Y., Feng, X., & Xiang, C. 2013, GeoRL, 40, 1457
Shen, F., Wu, S. T., Feng, X., & Wu, C.-C. 2012, JGR, 117, 11101
Shiota, D., & Kataoka, R. 2016, SpWea, 14, 56
Taktakishvili, A., Kuznetsova, M., MacNeice, P., et al. 2009, SpWea, 7, S03001
Titov, V. S., & Démoulin, P. 1999, A&A, 351, 707
Titov, V. S., Török, T., Mikic, Z., & Linker, J. A. 2014, ApJ, 790, 163
Tóth, G., Sokolov, I. V., Gombosi, T. I., et al. 2005, JGR, 110, 12226
Totten, T. L., Freeman, J. W., & Arya, S. 1995, JGR, 100, 13
Tsurutani, B. T., Smith, E. J., Gonzalez, W. D., Tang, F., & Akasofu, S. I. 1988, JGR, 93, 8519
Usmanov, A. V., & Dryer, M. 1995, SoPh, 159, 347
Vourlidas, A., Buzasi, D., Howard, R. A., & Esfandiari, E. 2002, in ESA Special Publication 506, Solar Variability: From Core to Outer Frontiers, ed. A. Wilson (Noordwijk: ESA Publications), 91
Wu, C.-C., Dryer, M., & Wu, S. T. 1996, AnGeo, 14, 383
Wu, C. C., Fry, C. D., Dryer, M., et al. 2007, AdSpR, 40, 1827
Wu, S. T., Guo, W. P., Michels, D. J., & Burlaga, L. F. 1999, JGR, 104, 14789
Wu, S. T., & Wang, J. F. 1987, CMAME, 64, 267
Xie, H., Ofman, L., & Lawrence, G. 2004, JGR, 109, A03109